

ABSTRACT

Title of Document: EXPERIMENTAL AND NUMERICAL
CHARACTERISTICS OF SOIL RESPONSE
TO INTENSE HEATING

Xiaoxi Luo, Master of Science, 2008

Directed By: Professor André Marshall, Department of Fire
Protection Engineering; and
Professor Deborah Goodings, Department of
Civil and Environmental Engineering

This work investigates the thermal transient response of different soils when exposed to intense heat flux. A special porous media code, TOUGH2, is applied for numerical analyses. Improvements are made to previous experimental facilities, and new experimental results are used to characterize the heat and mass transfer physics in the soil and verify simulations. A two-zone structure exists for the coarse sand, namely a liquid zone on top and a two-phase zone at bottom. A large convection cell is developed within the liquid zone. A two-zone structure is also observed in the fine sand. However, at later times the soil begins to dry out, and develops a vapor zone below the two-phase zone. The lower permeability in the fine sand tends to suppress convection, increase pore water pressure and temperatures. Finally, a full scale tunnel simulation is conducted to provide insight into the application of soil response during tunnel fires.

EXPERIMENTAL AND NUMERICAL CHARACTERISTICS OF SOIL
RESPONSE TO INTENSE HEATING

By

Xiaoxi Luo

Thesis submitted to the Faculty of the Graduate School of the
University of Maryland, College Park, in partial fulfillment
of the requirements for the degree of
Mater of Science
2008

Advisory Committee:
Professor André Marshall, Chair
Professor Deborah Goodings
Professor Frederick Mowrer

© Copyright by
[Xiaoxi Luo]
[2008]

Acknowledgements

This work has been funded by the National Science Foundation under Grant No. 0331332.

My foremost thanks and sincere appreciation goes to my advisors, Prof. André Marshall and Prof. Deborah Goodings, for their wonderful guidance, wisdom and patience. Every little step of my work would not be possible without their support and encouragement.

I am also grateful for all the help that Xianxu Hu gave me. Her previous amazing work always inspires me to do my best. Special thanks also go to Ning Ren, Yinghui Zheng and Lei Wang, for making my time at FETS lab much easier than I ever thought.

I would like to thank all the professors, staff and fellow students in Department of Fire Protection Engineering. I would not have such a wonderful and memorable study experience at University of Maryland if it was not for you.

Last but not the least, I would like to express my sincere thanks to my husband and parents, for their unconditional love, encouragement and belief all through the work.

Table of Contents

Acknowledgements.....	ii
Table of Contents.....	iii
List of Tables	iv
List of Figures	v
Nomenclature.....	viii
Chapter 1: Introduction	1
1.1 Motivation.....	1
1.2 Literature Review.....	3
1.2.1 Natural Convection and Boiling in Porous Media.....	3
1.2.2 Tunnel Fire Scenario Investigation.....	6
1.3 Objectives	7
Chapter 2: Approach	10
2.1 Experimental Methodologies	10
2.1.1 Test Matrix.....	10
2.1.2 Soil Properties.....	11
2.1.3 Improvements Made to Initial Experimental Setup.....	12
2.2 Simulation Approach	14
2.2.1 Conservation of Equations.....	14
2.2.2 Numerical Problem Definition.....	17
Chapter 3: Results and Analysis	19
3.1 Saturated Coarse Sand Experimental and Simulated Results	19
3.1.1 15 kW/m ² Incident Heat Flux	21
3.1.2 25 kW/m ² Incident Heat Flux	24
3.1.3 35 kW/m ² Incident Heat Flux	26
3.2 Saturated Fine Sand Experimental and Simulated Results	28
3.2.1 15 kW/m ² Incident Heat Flux	29
3.2.2 25 kW/m ² Incident Heat Flux	32
3.2.3 35 kW/m ² Incident Heat Flux	36
3.3 Comparison of the Response of Coarse and Fine Sand	37
3.4 Tunnel Fire Simulation	39
Chapter 4: Conclusions	42
Bibliography	44

List of Tables

Table 1 PIARC recommendations for different types of fire scenarios [26]	9
Table 2 Summary of car and wood crib fire tests in tunnels [24]	8
Table 3 Summary of pool fire tests in tunnels [24].....	9
Table 4 Test matrix	10
Table 5 Soil effective diameter	12
Table 6 Soil properties	12
Table 7 Comparison of vapor front propagation speed for coarse/fine sand	38
Table 8 Comparison of TOUGH2 excess pore water pressure change, saturation degree of coarse/fine sand.....	38

List of Figures

Figure 1 Experiment apparatus	13
Figure 2 Experimental setup schematics.....	14
Figure 3 Temperature and fluid velocity field for the saturated coarse sand when $\dot{q}'' = 25 \text{ kW/m}^2$ @ 3600 s	20
Figure 4 Temperature and fluid velocity field for the saturated coarse sand when $\dot{q}'' = 25 \text{ kW/m}^2$ @ 7200 s	20
Figure 5 TOUGH2 simulation of centerline temperature for the saturated coarse sand soil column compared with experiments ($\dot{q}'' = 15 \text{ kW/m}^2$).....	23
Figure 6 TOUGH2 simulations of the centerline vapor front for the saturated coarse sand soil column compared with experiments ($\dot{q}'' = 15 \text{ kW/m}^2$).....	23
Figure 7 TOUGH2 simulation of coarse sand excess pore water pressure change, saturation degree and temperature at the location of 0.2 m above the base ($\dot{q}'' = 15 \text{ kW/m}^2$). ..	24
Figure 8 TOUGH2 simulation of centerline temperature for the saturated coarse sand soil column compared with experiments ($\dot{q}'' = 25 \text{ kW/m}^2$).....	25
Figure 9 TOUGH2 simulations of the centerline vapor front for the saturated coarse sand soil column compared with experiments ($\dot{q}'' = 25 \text{ kW/m}^2$).....	26
Figure 10 TOUGH2 simulation of coarse sand excess pore water pressure change, saturation degree and temperature at the location of 0.2 m above the base ($\dot{q}'' = 25 \text{ kW/m}^2$). ..	26
Figure 11 Comparison of experimental centerline temperature profiles with 35 kW/m ² and 25 kW/m ² incident heat flux	27
Figure 12 Comparison of TOUGH2 centerline temperature profiles with 35 kW/m ² and 25 kW/m ² incident heat flux	28

Figure 13 Experimental centerline temperature for the saturated coarse sand soil column with $\dot{q}'' \approx 50 \text{ kW/m}^2$	28
Figure 14 Temperature and fluid velocity field for the saturated fine sand.....	30
Figure 15 Temperature and fluid velocity field for the saturated fine sand.....	30
Figure 16 TOUGH2 simulation of centerline temperature for the saturated fine sand soil column compared with experiments ($\dot{q}'' = 15 \text{ kW/m}^2$).....	31
Figure 17 TOUGH2 simulations of the centerline vapor front for the saturated fine sand soil column compared with experiments ($\dot{q}'' = 15 \text{ kW/m}^2$).....	31
Figure 18 TOUGH2 simulation of fine sand excess pore water pressure change, saturation degree and temperature at the location of 0.01m above the base ($\dot{q}'' = 15 \text{ kW/m}^2$)	31
Figure 19 TOUGH2 simulation of fine sand excess pore water pressure change, saturation degree and temperature at the location of 0.2 m above the base ($\dot{q}'' = 15 \text{ kW/m}^2$) .	32
Figure 20 TOUGH2 simulation of centerline temperature for the saturated fine sand soil column compared with experiments ($\dot{q}'' = 25 \text{ kW/m}^2$).....	34
Figure 21 TOUGH2 simulations of the centerline vapor front for the saturated fine sand soil column compared with experiments ($\dot{q}'' = 25 \text{ kW/m}^2$).....	35
Figure 22 TOUGH2 simulation of fine sand excess pore water pressure change, saturation degree and temperature at the location of 0.01m above the base ($\dot{q}'' = 25 \text{ kW/m}^2$)	35
Figure 23 TOUGH2 simulation of fine sand excess pore water pressure change, saturation degree and temperature at the location of 0.2m above the base ($\dot{q}'' = 25 \text{ kW/m}^2$) ...	35
Figure 24 TOUGH2 simulation of centerline temperature for the saturated fine sand soil column compared with experiments ($\dot{q}'' = 10 \text{ kW/m}^2$).....	36
Figure 25 TOUGH2 simulations of the centerline vapor front for the saturated fine sand soil column compared with experiments ($\dot{q}'' = 10 \text{ kW/m}^2$).....	36

Figure 26 TOUGH2 simulation of centerline temperature for the saturated fine sand soil column compared with experiments ($\dot{q}'' = 35 \text{ kW/m}^2$).....	37
Figure 27 TOUGH2 tunnel model	39
Figure 28 Coarse sand tunnel lining temperature field	40
Figure 29 Fine sand tunnel lining temperature field	40
Figure 30 Fine sand pressure history at the tunnel ceiling	40

Nomenclature

A	Area, m ²
c_p	Specific enthalpy, kJ/kg-K
D	Diameter of the soil particle, mm
\bar{g}	Gravity acceleration, m/s ²
H	Height, m
h	Specific enthalpy in TOUGH2 approach, kJ/kg
k	Thermal conductivity of the phase, W/m-K
k_{eff}	Effective thermal conductivity of the fluid mixture, W/m-K
k_{rl}	Relative permeability of the liquid phase
k_{rv}	Relative permeability of the vapor phase
K	Intrinsic permeability of the porous medium, m ²
L	Width of the porous medium layer, m
m	Mass, kg
n	The direction normal to a surface in equations (2-17) and (2-18)
P	Pressure, Pa
	Perimeter in equation (2-15)
p_c	Capillary pressure, Pa
\dot{q}''	Heat flux, kW/m ²
S	Liquid saturation
S_{lr}	The residual saturation of the liquid phase

S_{ls}	The maximum saturation of the liquid phase
S_{gr}	The residual saturation of the gas phase
T	Temperature, K
t	Time, s
\bar{v}	Darcy velocity, m/s
\bar{v}_n	Darcy velocity normal to a surface, m/s
\vec{V}	Physical velocity, m/s
V	Volume, m ³
w	Residual water content, kg
x	Coordinate
y	Coordinate
	Moisture content in equation (2-14)
z	Coordinate

Greek letters

φ	Porosity of the porous medium
λ	Effective thermal conductivity of the porous medium, W/m-K
ρ	Density, kg/m ³
μ	Dynamic viscosity, N-s/m ²
σ	Overburden pressure, N/m ²
σ_{eff}	Effective normal stress, N/m ²

Subscripts

l	Water liquid
s	Solid matrix
v	Water vapor
∞	Ambient
BH	Before heating
eff	Effective

Chapter 1: Introduction

Serious tunnel fire incidents have brought up more research and investigations of tunnel fire safety issues. Issues such as suppression, ventilation, tenability and computer model development for tunnel fire applications have been addressed. However, little attention has been given to the role that soil may play in structural safety of embedded structures exposed to accidental fires. This chapter introduces the motivation and objective of this study, and reviews the previous research work related to the project.

1.1 Motivation

Fires in tunnels usually involve intense heat flux and long duration, which cause tragic consequences including death, property loss and potentially severe damage to the tunnel infrastructures.

In 1979, Nihonzaka (Japan) tunnel fire lasted for 159 hrs, resulting in 7 deaths, and a damage of 127 trucks and 46 cars [1]. In 1995 a fire caused by an underground train in Baku (Azerbaijan) resulted in death of 300 people [2]. In 1999, the fire in Mont Blanc (France-Italy) tunnel was responsible for 39 deaths and damage to 24 vehicles [3]. In 2001, a fire caused by the collision of two heavy goods vehicles in the St. Gotthard tunnel (Switzerland) killed 11 people, destroyed 23 vehicles and resulted in tunnel collapse over 250 m. In the same year, Howard St. tunnel (USA) fire lasted for 48 hrs and damaged a major east coast internet communication link that ran through the tunnel, which slowed internet service around the US for several hours [4].

In the event of a fire, the soil layer may play an active role in the deterioration of the structural stability. Yong [5] at the University of Maryland conducted a set of

experiments studying the response of a 1.5 m high soil column heated from the bottom. In the experiments, the centerline temperatures and pore water pressures at different elevations were measured for different types of saturated soils. He found that a liquid zone existed above an underlying two-phase layer at the onset of boiling in his experiments. The leading front of the two-phase zone propagated upward as time increased. This propagation speed in the coarse sand was about 2 times that of the fine sand. Furthermore, there was a significant increase in the pore water pressure in the finer-grained saturated soil with low permeability. Campanella and Mitchell [6] concluded that heat-induced increases in pore water pressure in soil were directly related to the initial effective stress. This would mean that the modest excess pore water pressure fluctuations recorded in these experiments may translate to very substantial values when deep, saturated soil with a greater initial effective stress, is heated to the temperatures developing in these experiments.

Yong's research provided insights into soil transport behavior during tunnel fires. However, the difference of geometry between the experimental setup and the actual tunnels geometry limited the analysis. Therefore, Hu [1] at the University of Maryland established FLUENT and TOUGH2 numerical models and verified them with Yong's experimental data. Her research proved that capillary effects and relative permeability must be considered in the numerical model. TOUGH2 proved to be more suitable for this analysis. Reasonable qualitative agreement was achieved between 2-D TOUGH2 results and Yong's experimental data, regarding centerline temperature profiles, the vapor front propagation and the maximum excess pore water pressure.

Based on Yong and Hu's research, the motivation of this thesis is to further understand the physics and mechanics of the soil response to intense heat flux by refining the experiments and numerical analyses. The numerical simulation tool is also evaluated through comparisons of the experiments and simulation. Finally, soil response to fires in a realistic 2-D geometry is explored using TOUGH2.

1.2 Literature Review

1.2.1 Natural Convection and Boiling in Porous Media

When heated, the temperature change of the fluid media within saturated porous media or unsaturated porous media may cause a change in the fluid density. As a result, natural convection may be expected within the porous media. Several studies were focused on the pure convection problem. Bau [8] conducted experimental studies for a vertical circular cylinder containing a saturated porous media which was heated from below and cooled from above. The critical Rayleigh number was involved for determining the onset of convection. In his experiments, no boiling occurred. An 'S-shaped' curve was observed from the centerline temperature profile. The experimental and analytical prediction results were in reasonable agreement and strongly suggested that the convective motion of slender cylinders (large aspect ratios) was in the form of a single non-axisymmetric cell. It was concluded that natural convection occurred in porous media with higher permeability and that the non-axisymmetric single cell convection was the preferred mode for a slender circular cylinder. This research provided good insights into the natural convection phenomena in porous media.

When the saturated soil is exposed to intense heat flux, boiling may occur. A significant number of theoretical and numerical studies have been conducted regarding

this issue. Bau [7, 9] assumed an isothermal condition for the two-phase zone. With this simplification, he developed a simple 1-D steady state model to predict the height of the two-phase zone, the dry-out heat flux, and a necessary condition for the formation of a two-phase zone. However, he did not consider capillary effects. Faust [10] and Roberts [11] conducted numerical analyses for fluid flow and energy transport in porous hydrothermal systems, also neglecting capillary effects and considering the pressure-enthalpy correlation for pure water to determine water liquid/vapor enthalpy. Also neglecting capillary effects, separate flow model (SFM) was introduced to saturated porous media boiling and convection modeling by Ramesh [12, 13, 14]. His algorithm solved equations in both the liquid and two-phase regions. He was able to track the location of interface between the two zones by using a moving boundary approach. The finite difference control volume method was used to discretize these equations.

Wang et al. [15, 16, 17] numerically simulated a 2-D problem of boiling with thermal convection in a porous media layer heated from below by applying a two-phase mixture model and considering capillary effects. In order to consider capillary effects, a fixed grid was employed to avoid tracking the moving interface between the liquid and two-phase regions explicitly. The conservation equations of mass, momentum and energy were formulated for the two-phase mixture. Specifically, they utilized the error vector propagation method to solve the Poisson type pressure equation, and applied the control volume based finite difference scheme for the energy equation. Good agreements were achieved for the numerical results and the experimental investigations. Four different flow patterns observed in the experiments were successfully predicted by the model. Furthermore, Wang [17] extended this single-component multiphase model to a general

multi-component multi-phase model. The capillary effects were also considered in Udell's study [18, 19]. Udell provided a steady state 1-D model to predict the heat and mass transfer within the two-phase zone. The two-phase zone was considered to be isothermal to simplify the analysis. He evaluated the length of the two-phase zone. The model predicted a decreasing two-phase zone length with increasing heat flux, which agreed well with his experimental data. Furthermore, from the analysis of thermodynamic equilibrium between phases he found both vapor and liquid within the two-phase zone were superheated. A critical dry-out heat flux model was also given. He concluded that the effect of capillarity in porous media saturated with both vapor and liquid phases was responsible for the countercurrent flow of the two phases, which made the heat transfer process more efficient. In addition, the two-phase zone length was longer for basally heated systems and shorter if heated from above. Shi [20, 21] presented 1-D and 2-D expressions of the phase change (without dry-out) rate in his theoretical models of boiling heat transfer within the homogeneous porous layers and numerically predicted the critical heat flux, temperature distribution, etc. with and without the presence of chimneys. Only one empirical constant for the evaporation rate for phase change inside the porous media was introduced. Ulm's research [22, 23] explored soil response to the intense, prolonged heating, typical of what may occur in a tunnel fire, starting from simple 1-D soil column experiments to understand the mechanics of the behavior, and using that knowledge, to develop and train a numerical model with the eventual capability to predict more complex, more realistic full scale response.

Several experimental studies also have been conducted regarding the boiling problem within the porous media. Bau [4, 6] measured the temperature distribution for

boiling process in the porous media under steady state. He found that boiling could occur before or after natural convection. Under boiling but without dry-out, a quasi-isothermal two-phase zone (liquid and vapor) adjacent to the heating surface existed in the porous media. The height of the two-phase zone increased with the heat flux. Above the two-phase zone, a liquid zone was observed as either conduction dominated if no natural convection occurred or convection dominated if natural convection existed. Udell [7, 8] also carried out steady state experiments in a short sand column for top heated and horizontally heated cases. With dry-out, he found a stable three-zone structure which included (from top to bottom) a superheated vapor zone, a two-phase zone and a liquid zone. The vapor zone was conduction dominated. The two-phase convection zone was nearly isothermal and exhibited a countercurrent flow of liquid to the heated end and vapor to the cooled end. The compressed liquid zone was also conduction dominated. The length of the two-phase zone decreased with increasing heat flux.

The previous research has made significant progresses for problems involving boiling and convection in the porous media, however relatively little attention has been given to the non-steady soil transient behavior when exposed to a severe tunnel fire. Furthermore, few results about the vapor front propagation and the excess pore water pressure in the soil were reported.

1.2.2 Tunnel Fire Scenario Investigation

In § 1.1, examples of several catastrophic fires were presented. A body of fire research is available to provide insight into these fires. These researches provide information regarding the size and duration of fires in realistic geometries. The size, duration and geometry are very important factors in determining the thermal load to the

tunnel and its surrounding. Carvel [24] carried out a literature review to characterize the heat release rate (HRR) from tunnel fires and presented a method to estimate HRR considering tunnel geometry (especially width) and ventilation velocity. The fires in tunnels appeared to be significantly more severe than fires in the open air. The car fires he reviewed have HRR ranging from 1.5 MW to 6.0 MW. He also reviewed the fuel effects (e.g. wood crib, pool fires), fire sizes and testing tunnel geometries. Tunnel fire tests and basic characteristics are summarized in Table 1 and Table 3. Ingason [25] conducted scaled railcar fire tests. The large scale railcar experimental data he reviewed showed a peak HRR from 7 MW to 43 MW. The peak HRR he measured when all the railcar windows opened was between 36 MW and 47 MW. The peak HRR he measured when all the railcar windows closed was less than 3.5 MW. Megret [26] summarized the empirical recommendation of the fire characteristics for different types of fire scenarios in road tunnels from the World Road Association (Permanent International Association of Road Congresses) PIARC, as listed in Table 2. NIST [27] conducted FDS analyses for Howard tunnel fire, which happened in Baltimore, Maryland, 2001. In the simulation, the geometry of Howard tunnel was 8.2 m in width and 6.7 m in height, with fire sizes of 20 MW and 50 MW, and only natural ventilation was provided. For the 20 MW test, the gas temperature over the fire reached approximately 300 °C, whereas for the 50 MW test, the temperature reached 800 °C.

1.3 Objectives

The objective of the study is to characterize transport process in the soils exposed to intense heat. Basally heated soil column experiments and simulations are conducted to evaluate this response. The experiments follow the work conducted by Yong [5]. Yong

measured the centerline temperatures and pore water pressures for a column of basally heated saturated and unsaturated soils. The simulations follow the research by Hu [1]. Hu used a porous media CFD code, TOUGH2, capable of simulating hydro-thermal problems. The specific objectives of this study are to:

- Improve the experimental setup and evaluate soil response over a range of grain sizes (i.e. soil permeability). The refined experiments provide a clearer view of the dominant physics and transport mechanisms that govern the behavior of soil subjected to intense heat fluxes.
- Refine TOUGH2 soil column simulations. The comparison with experiments is used to evaluate the simulation tool's ability to predict the soil response during fires. The simulations provide extensive information within the soil matrix which is not available from measurements.
- Explore the response of soil surrounding a fired tunnel with a realistic geometry using the validated CFD tool, TOUGH2.

Table 1 Summary of car and wood crib fire tests in tunnels [24]

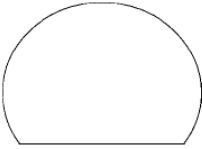


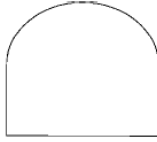
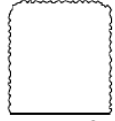
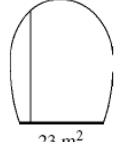
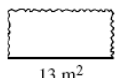
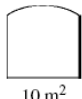
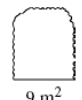
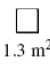
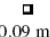
Tunnel	Tunnel Shape and Size	Fire Type	Dimensions
Des Monts three lane road tunnel France		Private Van	1.8 m wide 4.0 m long 1.6 m high (estimated)
Abandoned mine tunnel at Repparfjord near Hammerfest, Norway		Wooden Crib	0.8 m wide 3.2 m long 1.2 m high
		Renault Espace Car	2.1 m wide 4.5 m long 1.8 m high
Blasted rock tunnel used by FOA, Sweden		Wooden Cribs	0.7 m wide 0.7 m long 0.5 m high
		Fiat 127 Car	1.5 m wide 3.6 m long 1.3 m high

Table 2 PIARC recommendations for different types of fire scenarios [26]

Fire type	Passenger car	Three passenger cars	Van-bus	Heavy goods vehicle	Petrol tanker
Total heat release rate (MW)	4	8	15	30	100
Smoke flow rate (m ³ /s)	20	30	50	80	200–300

Table 3 Summary of pool fire tests in tunnels [24]

Tunnel	Tunnel Shape and Size	Pool Fuel	Pool Shape	Pool Size
Abandoned two lane road tunnel near Charleston, West Virginia, USA	 56 m ²	Diesel	Rectangular	9 m ² 22 m ²
Abandoned mine tunnel at Repparfjord near Hammerfest, Norway	 25–30 m ²	Heptane	Circular	1 m ² 3 m ²
Abandoned railway tunnel at Ofenegg, Switzerland	 23 m ²	Petrol	Rectangular	6.65 m ² 47.5 m ² 95 m ²
Mine roadway tunnel at Londonderry, Australia	 13 m ²	Kerosene	Circular	0.26 m ² 0.78 m ² 3.14 m ²
Large scale fire gallery at INERIS, France	 10 m ²	Heptane	Circular	1.0 m ²
Blasted rock tunnel used by FOA, Sweden	 9 m ²	Heptane	Square	0.42 m ² 0.64 m ²
Model scale tunnel at SP, Sweden	 1.3 m ²	Methanol	Rectangular	2.0 m ²
Lab scale wind tunnel at Fire Research Institute, Japan	 0.09 m ²	Heptane	Square	0.09 m ² 0.16 m ²
		Xylene	Square	0.09 m ²
		Methanol	Square	0.16 m ²
		Heptane	Circular	0.018 m ²
		Methanol	Circular	0.008 m ² 0.018 m ² 0.031 m ² 0.049 m ²

Chapter 2: Approach

This chapter introduces the experimental setup and improvements, soil properties, as well as the conservation equations used in the numerical analyses.

2.1 Experimental Methodologies

2.1.1 Test Matrix

In order to further understand the response of different saturated soils to various heat fluxes, experiments with three different basal heat flux boundary conditions are conducted for both the coarse sand and the fine sand. Furthermore, two sets of experiments are conducted for each soil and heat flux combination to address test repeatability. In all, 12 tests are conducted. Table 4 provides a summary of tested soil type, heat flux and measurements performed in the experiments.

Table 4 Test matrix

S/N	Type of media tested	Incident heat flux [kW/m ²]	Net basal heat flux [kW/m ²]	Measurements
1	Saturated coarse sand	15	15	Incident heat flux; heater/base temperature; pore water pressure at different elevations; temperature at different elevations.
2		25	25	
3		35	35	
4	Saturated fine sand	15	8.3	Incident heat flux; heater/base temperature; pore water pressure at different elevations; temperature at different elevations.
5		25	13.6	
6		35	15.5	

2.1.2 Soil Properties

All the sand is commercially produced from the U.S. Silica Company in Berkeley Springs, WV. The coarse sand is grade #3 Q-ROK, and the fine sand is grade F-62. In order to achieve a more uniform grain size distribution, all soils have been filtered before application. For the coarse sand, #16 and #20 sieves are used to narrow down grain size to 0.85mm - 1.18mm. For the fine sand, #50 and #100 sieves are used to narrow down grain size to 150 μ m - 300 μ m.

In this case, the soil consists of nonuniform spheres, and the effective diameter D_{eff} can be calculated from the particle size distribution [1]:

$$D_{eff} = 100\% / \left[\sum (f_i / D_{avg,i}) \right] \quad (2-1)$$

where f_i = fraction of particles between two sieve sizes, large [L] and small [S]; and

D_{avg} = average particle size between two sieve sizes = $D_{Li}^{0.5} \times D_{Si}^{0.5}$. In both the coarse sand and fine sand, there are two size bands reported by the manufacturer within the filtered range. The details of the soil size distribution and effective diameter are reported in Table 5.

The ASTM Standard Test Method for Laboratory Determination of Water (Moisture) Content of Soil and Rock by Mass (Designation: D 2216–98) is used to determine the residual water content of the soil [5]. Soil porosity ϕ is determined by the following equation:

$$\phi = \frac{w / \rho_w}{w / \rho_w + (1 - w) / \rho_s} \quad (2-2)$$

where w is the residual water content, ρ_w is the density of water, ρ_s is the density of soil particles.

The intrinsic permeability of the soils can be estimated using Kozeny-Carmen formula as shown [1, 29]:

$$K = \frac{D_{eff}^2}{180} \times \frac{\phi^3}{(1-\phi)^2} \quad (2-3)$$

where K is the intrinsic permeability for the porous media. Table 6 lists the properties for different soil types.

Table 5 Soil effective diameter

	D_{L1}^* (mm)	D_{S1} (mm)	f_1	D_{ave1} (mm)	D_{L1} (mm)	D_{S1} (mm)	f_2	D_{ave2} (mm)	D_{eff} (mm)
Coarse	1.18	1.0	0.42	1.1	1.0	0.85	0.58	0.92	1.0
Fine	0.030	0.021	0.51	0.025	0.021	0.015	0.49	0.018	0.021

* D_{Li} is from manufacture data.

Table 6 Soil properties

Soil Type	Average porosity ϕ (%)	Permeability K (m ²)	Effective thermal conductivity, k_{eff} (W/m.K) [5]
Coarse	47	2.1×10^{-9}	2.24
Fine	39	4.0×10^{-11}	2.8

2.1.3 Improvements Made to Initial Experimental Setup

As illustrated in Figure 1 and Figure 2, a steel tube with a height of 1.5 m and a diameter of 0.1 m is used as the soil container. An 8 cm thick glass fiber insulation layer is installed outside of the soil column. Pressure and temperature measurement

instruments are inserted into the soil column to measure along the column centerline. The height of the soil layer is 1.2 m. There is a 0.1 m water layer above the soil layer to maintain soil saturation. The water layer opens to the ambient.

The following improvements have been done to the experimental setup:

- Both the coarse and the fine sand are filtered to achieve more uniform grain distribution before being filled into the column.
- Heat shields are installed around the heater and soil column to provide repeatable heat flux boundary conditions.
- Pressure transducers are carefully calibrated and verified by measuring hydrostatics pressure correctly.
- A heat flux gauge is installed at the base of the column, measuring incident heat flux from the radiant panel heater directly.
- The insulation layer is reinforced.
- An overflow tube is inserted at the top of the water layer. The amount of overflowed water during experiments is collected and measured.

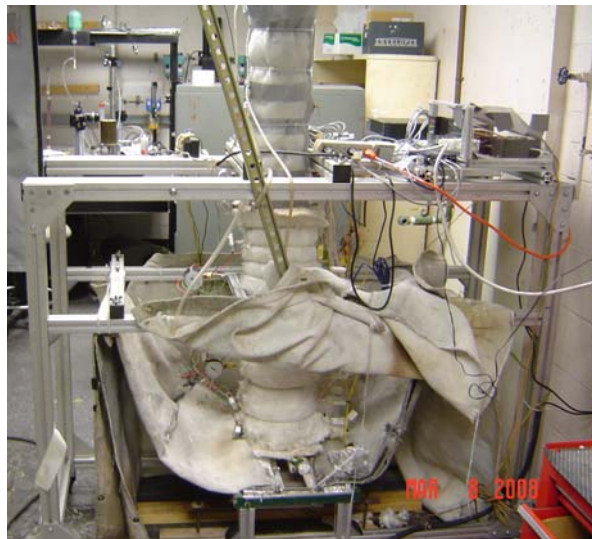


Figure 1 Experiment apparatus

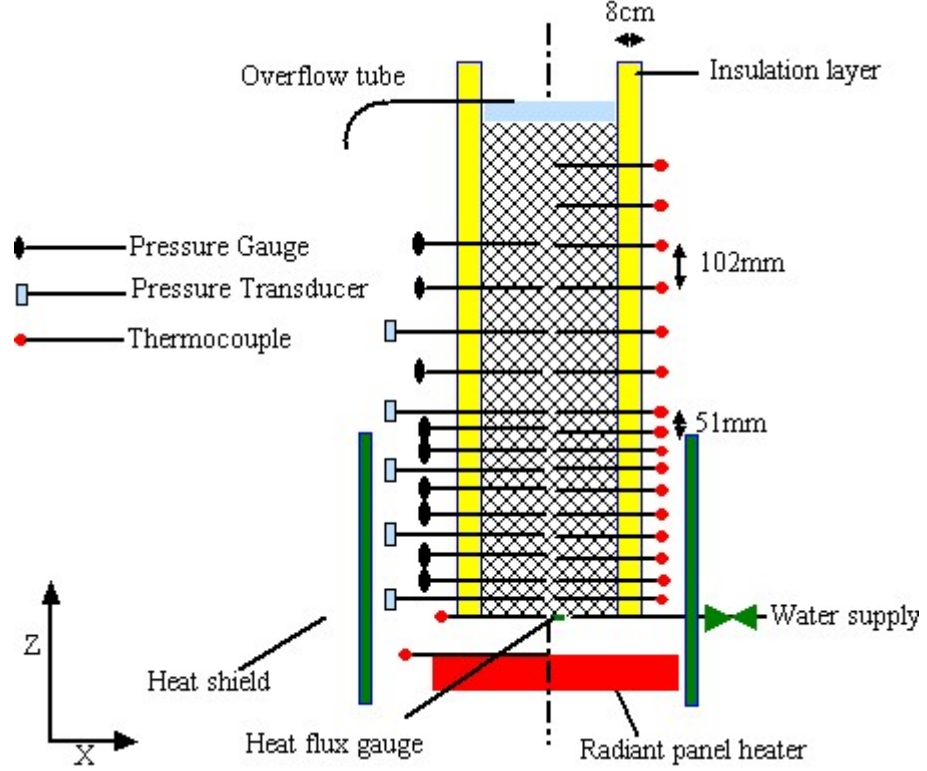


Figure 2 Experimental setup schematics

2.2 Simulation Approach

The following assumptions are introduced in order to simplify the problem [1]:

- 1) the porous media is isotropic;
- 2) the solid matrix is rigid;
- 3) at any point of the continuous media, the three phases are locally at thermal equilibrium ($T_s = T_l = T_v = T$);
- 4) mass diffusion between phases can be neglected.

2.2.1 Conservation of Equations

Based on the above assumptions, the basic mass and energy balance equations solved by TOUGH2 can be written as [30]:

Mass equation

$$\frac{\partial}{\partial t}(\phi S \rho_l + \phi(1-S)\rho_v) + \nabla \cdot (\rho_l \bar{v}_l + \rho_v \bar{v}_v) = 0, \quad (2-4)$$

and energy equation

$$\begin{aligned} & \frac{\partial}{\partial t}(\phi S \rho_l h_l + \phi(1-S)\rho_v h_v + (1-\phi)\rho_s c_{p,s} T) \\ & - \frac{\partial}{\partial t}(\phi S p_l + \phi(1-S)p_v) + \nabla \cdot (\rho_l h_l \bar{v}_l + \rho_v h_v \bar{v}_v) - \nabla \cdot (\lambda \nabla T) = 0 \end{aligned} \quad (2-5)$$

The multiphase version of Darcy's law

$$\bar{v}_l = -\frac{k_{rl} K}{\mu_l} (\nabla p_l - \rho_l \bar{g}), \quad (2-6)$$

$$\bar{v}_v = -\frac{k_{rv} K}{\mu_v} (\nabla p_v - \rho_v \bar{g}), \quad (2-7)$$

$$p_l = p_v + p_c. \quad (2-8)$$

In this analysis, van Genuchten-Mualem model [30] is used to estimate both the relative permeability and the capillary pressure. The van Genuchten-Mualem model of the relative permeability describes the relative hydraulic conductivity of each fluid phase based on the retention quantities (i.e., the effective degree of liquid saturation (S^* , \hat{S}), and the parameter, m , which is related to the shape of the retention curve) [1]. The relative permeability can be described as follows:

$$k_{rl} = \begin{cases} \sqrt{S^*} \left(1 - \left(1 - [S^*]^{\frac{1}{m}} \right)^m \right)^2 & \text{if } S_l < S_{ls} \\ 1 & \text{if } S_l \geq S_{ls} \end{cases}, \quad (2-9)$$

$$k_{rg} = \begin{cases} 1 - k_{rl} & \text{if } S_{gr} = 0 \\ (1 - \hat{S})^2 (1 - \hat{S}^2) & \text{if } S_{gr} > 0 \end{cases}, \quad 0 \leq k_{rl}, \quad k_{rg} \leq 1, \quad (2-10)$$

where

$$S^* = \frac{S - S_{lr}}{S_{ls} - S_{lr}}, \quad (2-11)$$

$$\hat{S} = \frac{S - S_{lr}}{1 - S_{lr} - S_{gr}}. \quad (2-12)$$

S_{lr} is the residual saturation of liquid phase, and S_{gr} is the residual saturation of vapor phase.

The van Genuchten-Mualem model for the capillary pressure is also based on S^* and m . And it is given by:

$$p_c = -p_0 \left(\left[S^* \right]^{\frac{1}{m}} - 1 \right)^{1-m}, \text{ subject to } -p_{\max} \leq p_c \leq 0, \quad (2-13)$$

where, p_0 is a reference pressure and p_{\max} is the negative capillary pressure when $S \rightarrow S_{lr}$.

The residual saturation of the liquid phase, S_{lr} , is an empirical quantity related to grain material and shape. Fredlund [31] determined that $S_{lr} \approx 0.1$ for glass beads, $S_{lr} \approx 0.15$ for volcanic sand, $S_{lr} \approx 0.2$ for fine sand and $S_{lr} \approx 0.45$ for Touchet silt loam.

The steam table equations used in TOUGH2 are based on the equations given by the International Formulation Committee (1967). The degree of liquid saturation, S , can be related to the steam moisture content y through the following equation:

$$y = \frac{m_l}{m_l + m_v} = \frac{\rho_l V_l}{\rho_l V_l + \rho_v V_v} = \frac{\rho_l S}{\rho_l S + \rho_v (1 - S)}. \quad (2-14)$$

To summarize, there are 15 unknowns variables in the analysis: ρ_l , ρ_v , S , \vec{v}_l , \vec{v}_v , k_{rl} , k_{rv} , p_l , p_v , p_c , μ_l , μ_v , h_l , h_v , T . Equations (2-4) - (2-10), (2-13), (2-14) and 6 steam table equations provide 15 equations so that the problem is closed mathematically.

2.2.2 Numerical Problem Definition

Based on the configuration of the experiment, a 2-D TOUGH2 porous media simulation is conducted. The 2-D geometry model is based on the assumption that the cylinder configuration is dominated by the transport in the z-direction, since the aspect ratio, H / L , is large. It is recognized that the convection behavior of the 2-D simulation is different from what occurs in the cylindrical experimental configuration. However, the details of convection effects are assumed to play a secondary role, compared with the dominant capillary and phase change transport processes. This assumption can be evaluated by comparing the simulations and experiments. Characteristic length in this problem is the column diameter D_c . The geometry of the 2-D model should meet the following correlation,

$$D_c = \frac{4A}{P} = \frac{4 * L_x * L_y}{2 * (L_x + L_y)} = 2L_x, \quad (2-15)$$

where A is the cross section area of the soil column, P is the perimeter of the column cross section, L_x is x direction dimension, and L_y is y direction dimension ($L_y \rightarrow \infty$ in the 2-D model). As determined from (2-15), L_x is a half of the column diameter, namely 0.05 m. In the following correlation, $L_x = L$.

The appropriate boundary and the initial conditions of the 2-D soil column model are:

$$z = H, \quad p = p_\infty = 1 \text{ atm}, \quad (2-16)$$

$$x = \pm \frac{L}{2}, \quad \frac{\partial T}{\partial n} = 0, \quad \vec{v}_n = 0, \quad (2-17)$$

$$z = 0, \quad -k \frac{\partial T}{\partial n} = \dot{q}'', \quad \vec{v}_n = 0, \quad (2-18)$$

$$t = 0, \quad T = T_{\infty}, \quad \vec{v} = 0. \tag{2-19}$$

Chapter 3: Results and Analysis

The results of experiments and TOUGH2 analyses are provided in this chapter. The analyses focus on the centerline temperature profiles, vapor front propagation speed, excess pore water pressure and saturation degree. Furthermore, full scale TOUGH2 model is developed to simulate soil response to tunnel fire.

3.1 Saturated Coarse Sand Experimental and Simulated Results

Complex heat and mass transfer phenomena are exhibited in the saturated coarse sand column when it is exposed to intense heat flux. As continuous heat is transferred to the soil matrix and fluid from the base, water vaporization, boiling, condensation, and natural convection occur, resulting in the excess pore water pressure.

Figure 3 and Figure 4 provide examples of the thermal transient dynamics in the soil column. TOUGH2 simulation results of the temperature and vapor/liquid velocity field of the saturated coarse sand media with 25 kW/m^2 incident heat flux are illustrated. There are two zones formed in the media, namely a liquid zone on the top and a two-phase zone on the bottom. In the two-phase zone, no dry-out has occurred. The temperature there is the boiling temperature. The vapor cools down as it moves toward the liquid zone, and eventually condenses. The condensate flows downward in the two-phase zone to compensate the mass loss due to the vapor movement. The vapor front propagates upward as time increases. The vapor front is defined at the lowest centerline location where the liquid saturation degree S equals 1. In other words, it is the leading edge of the two-phase zone along the centerline. In the liquid zone, a big convection cell

is developed, resulting in the velocity vortex and uneven temperature distribution in that region. Meanwhile, the convection cell propagates together with the vapor front.

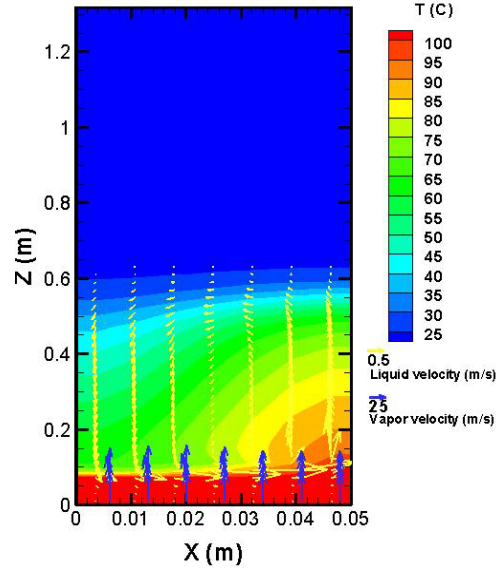


Figure 3 Temperature and fluid velocity field for the saturated coarse sand when $\dot{q}'' = 25\text{kW/m}^2$
@ 3600 s

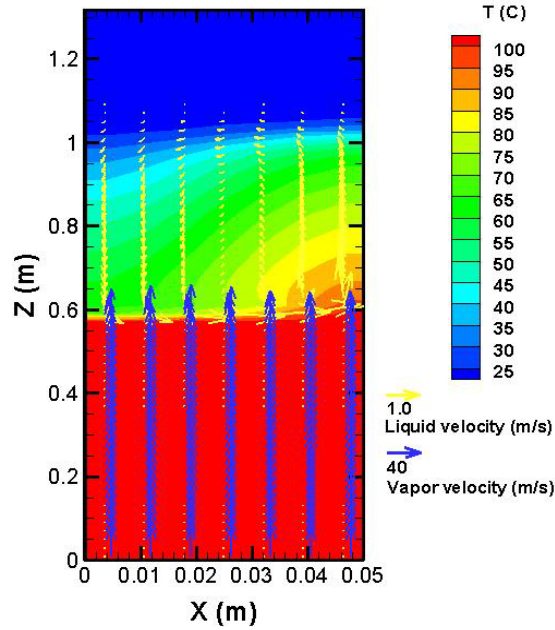


Figure 4 Temperature and fluid velocity field for the saturated coarse sand when $\dot{q}'' = 25\text{kW/m}^2$
@ 7200 s

Experimental results are provided in the following sections to characterize the effects of heat intensity and soil permeability on the transient dynamics and to evaluate the model performance at different conditions. Temperature measurements and vapor front propagation velocities are used for characterization and model verification, while more detailed quantities are available from the simulations.

3.1.1 15 kW/m² Incident Heat Flux

As shown in Figure 5, two sets of experiments are conducted with the boundary condition of 15 kW/m² incident heat flux, and the results show good repeatability. Furthermore, the experimental centerline temperature profile compares well with the TOUGH2 simulation results. Before boiling occurs in the two-phase zone at $t = 1.5$ hr, a strong convection cell develops gradually in the liquid zone. During its growing period, the centerline vapor front doesn't propagate. The fully developed convection cell is around 0.6 m high and it dominates one half of the soil column. After 1.5 hr, the centerline vapor front starts to propagate upward and the domain of the two-phase zone increases with time. In the experiments, the centerline vapor front propagates with a speed of 0.25 m/hr, while the TOUGH2 simulation provides a speed of 0.29 m/hr as shown in Figure 6. However it is noted that the experimental vapor front propagation is delayed relating to TOUGH2 simulation. Similar observation can be found in the 25 kW/m² incident heat flux case. It is caused by the following possible reasons: 1) the metal column has a certain heat capacity, and is not considered in TOUGH2 simulation; 2) heat loss through the insulation layer surrounding the column to the ambient environment. After 2.5 - 3.0 hr, the top of the convection cell is about to reach the top of the soil

column. The temperature distribution inside the soil column is strongly affected by the boundary condition from then on. Thus only data before that is considered in this analysis.

Figure 7 provides TOUGH2 time evolution of the pore water pressure, saturation degree and temperature at the location of 0.2 m above the base. Instead of showing absolute values, three normalized variables are introduced to better describe the physics.

The excess pore water pressure over effective normal stress before heating, $\frac{\Delta P}{\sigma_{eff_BH}}$, describes the ratio between the excess pore water pressure ΔP and the effective normal stress before heating σ_{eff_BH} . ΔP acts against σ_{eff} , which contributes to keeping the soil particles in place. The effective normal stress, σ_{eff} , and effective normal stress before heating, σ_{eff_BH} , are defined as following,

$$\sigma_{eff} = \sigma - P \quad (3-1)$$

$$= \sigma - (\rho_w * H * g + \Delta P)$$

$$= \sigma - \rho_w * H * g - \Delta P ,$$

$$\sigma_{eff_BH} = \sigma_{BH} - \rho_w * H * g , \quad (3-2)$$

where, σ is the overburden pressure, σ_{BH} is the overburden pressure before heating ,

P is the pore water pressure and ΔP is the excess pore water pressure. The overburden pressure, σ , is due to the combined weight of the soil matrix and the fluids which occupy the spaces within the soil matrix. After heating, σ is subject to change since the mass amount of fluid is about to change. (3-1) can be written as

$$\frac{\sigma_{eff}}{\sigma_{eff_BH}} = \frac{\sigma - \rho_w H g}{\sigma_{eff_BH}} - \frac{\Delta P}{\sigma_{eff_BH}} . \quad (3-3)$$

If it is assumed that σ does not change after heating and σ_{eff_BH} is a constant, then correlation (3-3) can be simplified as the following.

$$\frac{\sigma_{eff}}{\sigma_{eff_BH}} = 1 - \frac{\Delta P}{\sigma_{eff_BH}} \quad (3-4)$$

It is observed that when $\frac{\Delta P}{\sigma_{eff_BH}}$ equals unity, the overburden pressure, σ , equals the pore water pressure, P , which means there is no stress to hold soil particles together.

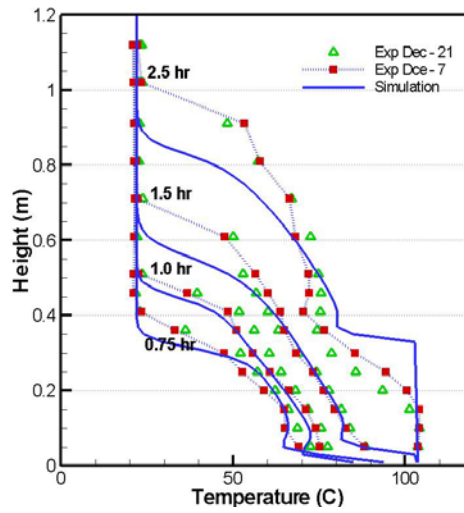


Figure 5 TOUGH2 simulation of centerline temperature for the saturated coarse sand soil column compared with experiments ($\dot{q}'' = 15 \text{ kW/m}^2$)

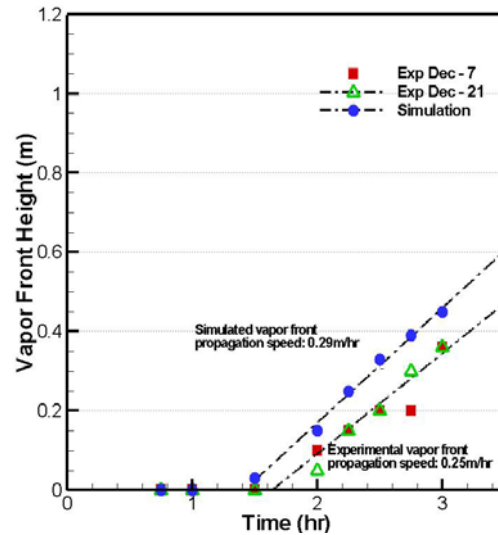


Figure 6 TOUGH2 simulations of the centerline vapor front for the saturated coarse sand soil column compared with experiments ($\dot{q}'' = 15 \text{ kW/m}^2$)

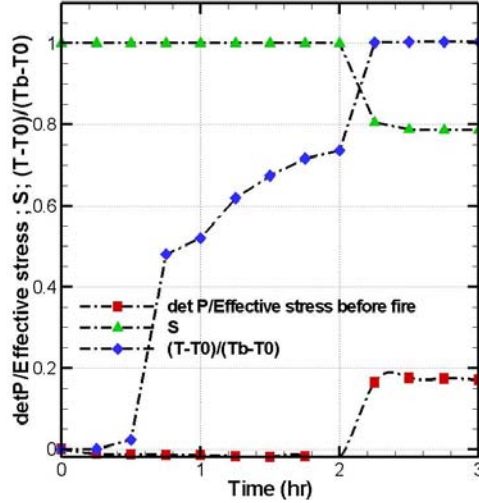


Figure 7 TOUGH2 simulation of coarse sand excess pore water pressure change, saturation degree and temperature at the location of 0.2 m above the base ($\dot{q}'' = 15 \text{ kW/m}^2$)

The quantity, S , provides the degree of saturation ranging from 0 to 1. The

quantity, $\frac{(T - T_0)}{(T_b - T_0)}$, provides the ratio between local temperature and the boiling

temperature, ranging from 0 to 1 if there is no dry-out. T_0 is the ambient temperature,

$T_0 = T_\infty$. As shown in Figure 7, before $t = 2 \text{ hr}$, $\frac{(T - T_0)}{(T_b - T_0)}$ gradually increases but is still

smaller than 1, while S remains 1 and no pressure change occurs. During this period, the

solid column below 0.2 m is slowly heated up. When $t = 2.2 \text{ hr}$, $\frac{(T - T_0)}{(T_b - T_0)}$ changes into 1,

which indicates the initiation of vaporization. Meanwhile, S changes from 1 to 0.8 and

$\Delta P / \sigma_{eff_BH}$ changes from 0 to 0.17. The occurrence of boiling causes the pore water pressure to change.

3.1.2 25 kW/m² Incident Heat Flux

As shown in Figure 8, two sets of experiments with 25 kW/m² incident heat flux compares well with TOUGH2 simulation. The centerline vapor front is built up at $t = 1.0$

hr. At the same time, convection cell (0.5 m) is also developing in the liquid zone. As shown in Figure 9, the vapor front moves with a speed of 0.42 m/hr in experiments and 0.38 m/hr in TOUGH2 simulation. Comparing with 15 kW/m² case, the convection cell is slightly suppressed, however develops faster; the vapor front propagation speed is also higher. Figure 10 provides TOUGH2 time evolution of $\frac{\Delta P}{\sigma_{eff_BH}}$, S and $\frac{(T-T_0)}{(T_b-T_0)}$ at the location of 0.2 m above the base. Before $t = 1$ hr, $\frac{(T-T_0)}{(T_b-T_0)}$ is smaller than 1, while S remains 1 and no pressure change occurs. After $t = 1$ hr, $\frac{(T-T_0)}{(T_b-T_0)}$ changes to 1; S changes from 1 to 0.75; and $\frac{\Delta P}{\sigma_{eff_BH}}$ changes from 0 to around 0.19. S and $\frac{\Delta P}{\sigma_{eff_BH}}$ are slightly changed comparing with 15 kW/m² case; however they are not a strong function of the incident heat flux.

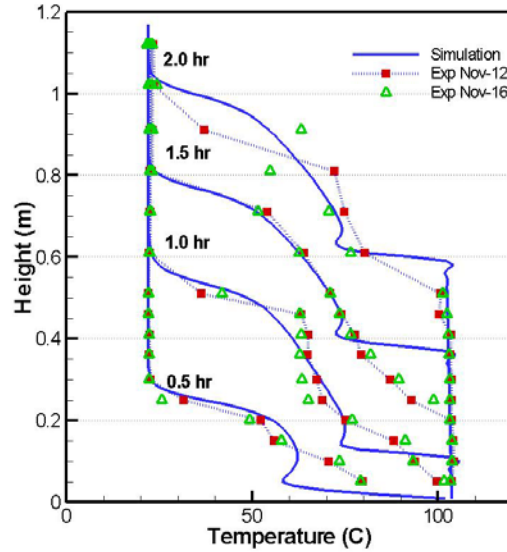


Figure 8 TOUGH2 simulation of centerline temperature for the saturated coarse sand soil column compared with experiments ($\dot{q}'' = 25$ kW/m²)

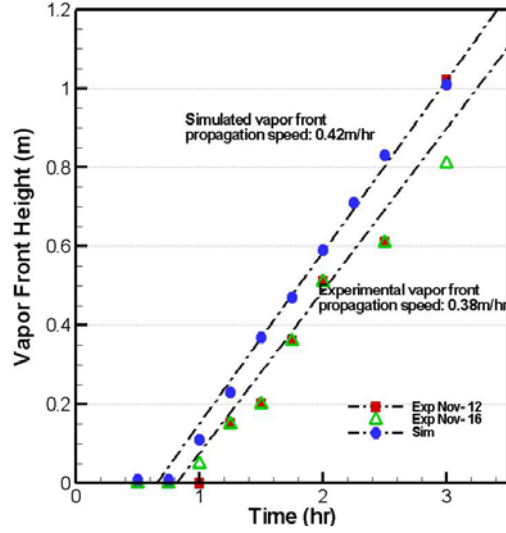


Figure 9 TOUGH2 simulations of the centerline vapor front for the saturated coarse sand soil column compared with experiments ($\dot{q}'' = 25 \text{ kW/m}^2$)

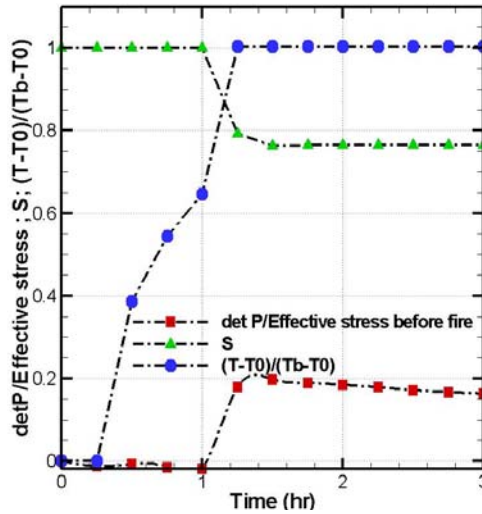


Figure 10 TOUGH2 simulation of coarse sand excess pore water pressure change, saturation degree and temperature at the location of 0.2 m above the base ($\dot{q}'' = 25 \text{ kW/m}^2$)

3.1.3 35 kW/m² Incident Heat Flux

Figure 11 and Figure 12 compares the experimental and TOUGH2 centerline temperature profiles with 35 and 25 kW/m² incident heat fluxes. Counter-intuitive results are observed. In simulations, a smaller convection cell and a faster vapor propagation speed are observed for the larger heat flux case. While in experiments, a large convection cell is developed for the 35 kW/m² cases and the vapor front propagates at almost the

same speed as the 25 kW/m^2 cases. The 35 kW/m^2 tests are the last cases conducted. After several sets of experiments, the excess pore water pressure might have changed the soil mechanical structure already. There might be channeling inside the soil column, which changes the porosity and permeability and provides fluid easier pathway. As a result, a very strong convection in the liquid zone is developed and the propagation of vapor front is slowed down. Hence the 35 kW/m^2 cases can not provide effective verification of TOUGH2 model. Furthermore, Figure 13 provides a set experimental test results, run with $\dot{q}'' \approx 50 \text{ kW/m}^2$. The results show a faster vapor front propagation, and smaller size of the convection cell, which agrees with the trend TOUGH2 provides.

To summarize, higher incident heat flux results in faster vapor front propagation. For the coarse sand, convection cell is developed together with the vapor front. Instead of only building up the two-phase zone, thermal energy is distributed to a broader region due to convection. So the tunnel lining made up of coarse sand does not generate extremely high temperature or pore water pressure in the event of fires.

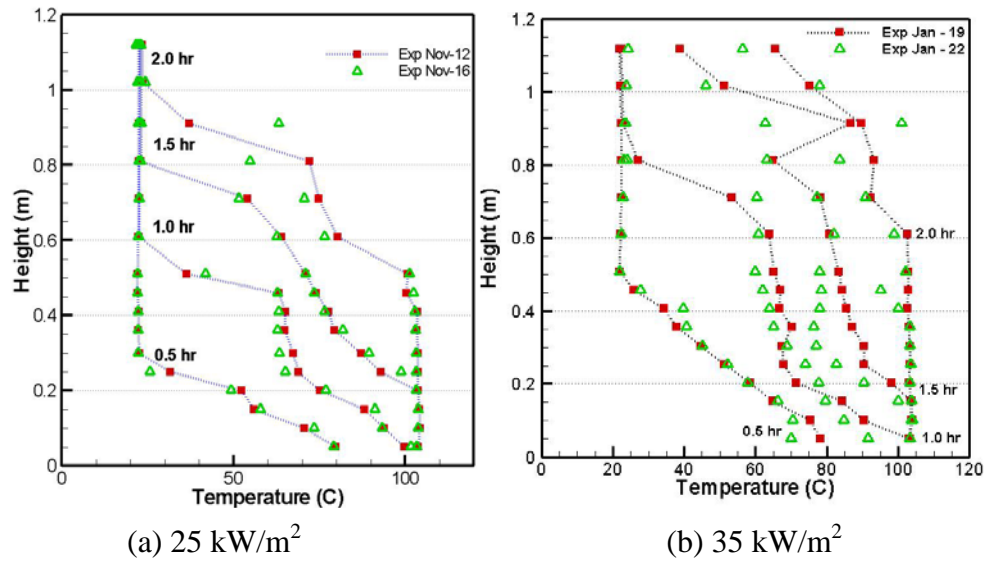


Figure 11 Comparison of experimental centerline temperature profiles with 35 kW/m^2 and 25 kW/m^2 incident heat flux

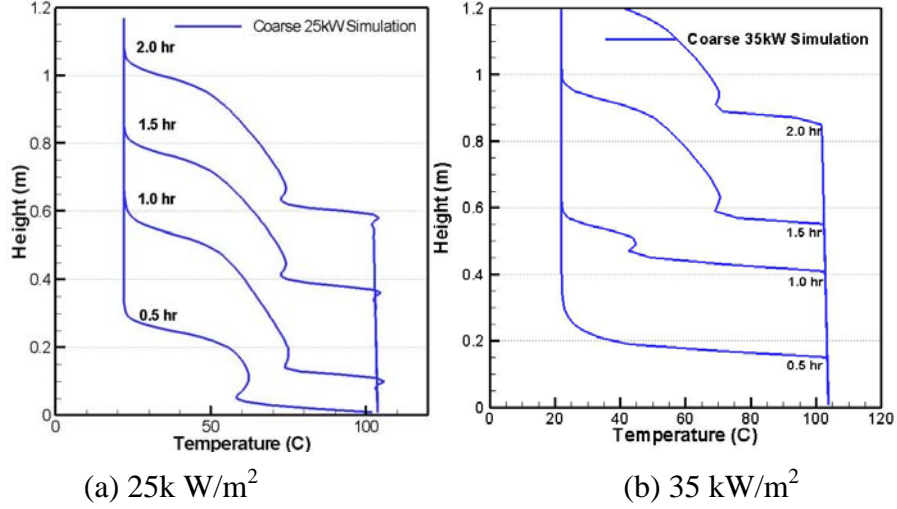


Figure 12 Comparison of TOUGH2 centerline temperature profiles with 35 kW/m² and 25 kW/m² incident heat flux

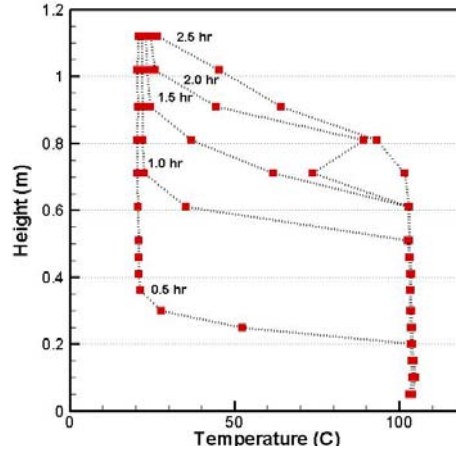


Figure 13 Experimental centerline temperature for the saturated coarse sand soil column with $\dot{q}'' \approx 50 \text{ kW/m}^2$

3.2 Saturated Fine Sand Experimental and Simulated Results

The following sections discuss the experimental and TOUGH2 simulated results for the thermal transient behavior of the fine sand. Different heat and mass transfer pattern is found in the fine sand cases. Figure 14 and Figure 15 illustrate TOUGH2 results for the temperature and velocity field of the fine sand at $t = 7200 \text{ s}/9000 \text{ s}$, with 25 kW/m^2 incident heat flux. When $t = 7200 \text{ s}$, a two-zone structure is formed, namely a liquid zone on the top and a two-phase zone on the bottom. In the two-phase zone, the

vapor moves straight upward and condenses when it reaches the liquid zone. Meanwhile, the cold liquid moves down to compensate the mass loss caused by the vapor movement. A current flow is formed by the upward vapor and downward liquid. Different from the coarse sand, a very steep temperature gradient exists at the interface of the two zones. No convection cells are observed in the liquid zone. The temperature distribution in the liquid zone is uniform except the interface region. In Figure 15, when $t = 9000$ s, a three-zone structure is formed, with a liquid zone on the top, a two-phase zone expanding further upward in the middle and a vapor zone on the bottom. Dry-out occurs in the vapor zone. The temperature there reaches 210°C .

3.2.1 15 kW/m^2 Incident Heat Flux

Good repeatability is obtained between the two sets of experiments under 15 kW/m^2 incident heat flux. Figure 16 compares the centerline temperature of TOUGH2 and experiments. The flat temperature curve indicates a steep temperature gradient between two zones. The vapor front is generated since 0.5 hr , much faster than the coarse sand. TOUGH2 gives a linear centerline vapor front propagation speed of 0.18 m/hr , and the experiments shows a speed of 0.17 m/hr before 3.5 hr . In experiments the vapor front decelerates propagation between 3.5 and 4.0 hr and builds up a “step” in Figure 17. Possible reasons are discussed in § 3.2.2.

Figure 18 and Figure 19 provide TOUGH2 time evolution of $\Delta P / \sigma_{\text{eff} - BH}$, S and $\frac{(T - T_0)}{(T_b - T_0)}$ at the location of 0.01 m and 0.2 m above the base. At the location of 0.01 m (Figure 18), vapor front reaches the local point since 0.5 hr . Temperature remains at boiling temperature. $\Delta P / \sigma_{\text{eff} - BH}$ is around 0.3 . Saturation degree gradually decreases as

more liquid vaporizes in the two-phase zone. Figure 19 depicts the vapor front propagation at the location of 0.2m. At $t = 1.5$ hr, the vapor front moves to the local position. Saturation degree decreases from 1 to around 0.6. The excess pore water pressure increases to 38% of the effective normal stress. Since no dry-out occurs, the temperature increases to boiling temperature and remains as that.

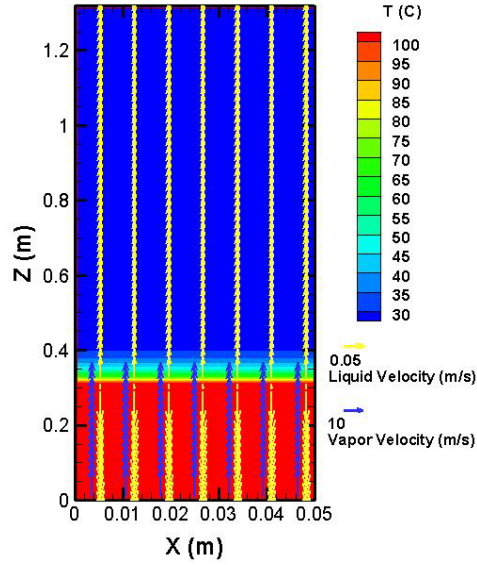


Figure 14 Temperature and fluid velocity field for the saturated fine sand when $\dot{q}'' = 25 \text{ kW/m}^2$ @ 7200 s

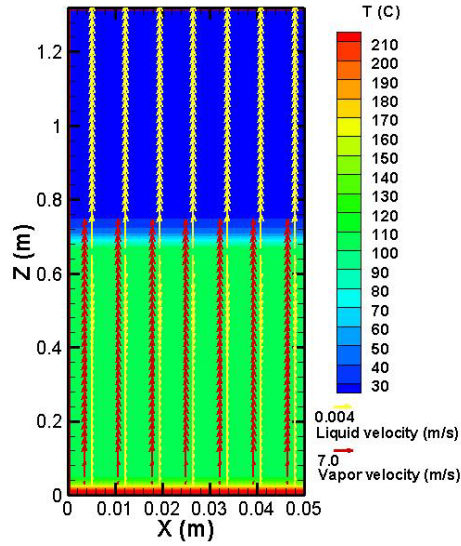


Figure 15 Temperature and fluid velocity field for the saturated fine sand when $\dot{q}'' = 25 \text{ kW/m}^2$ @ 9000 s

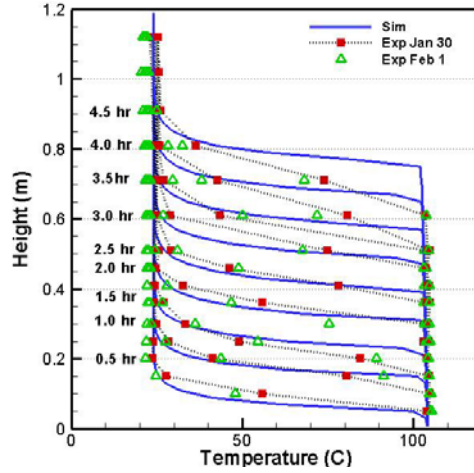


Figure 16 TOUGH2 simulation of centerline temperature for the saturated fine sand soil column compared with experiments ($\dot{q}'' = 15 \text{ kW/m}^2$)

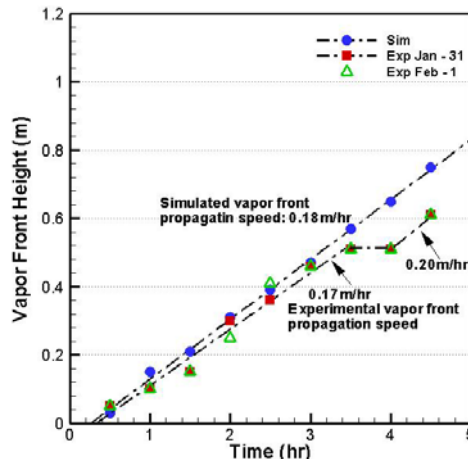


Figure 17 TOUGH2 simulations of the centerline vapor front for the saturated fine sand soil column compared with experiments ($\dot{q}'' = 15 \text{ kW/m}^2$)

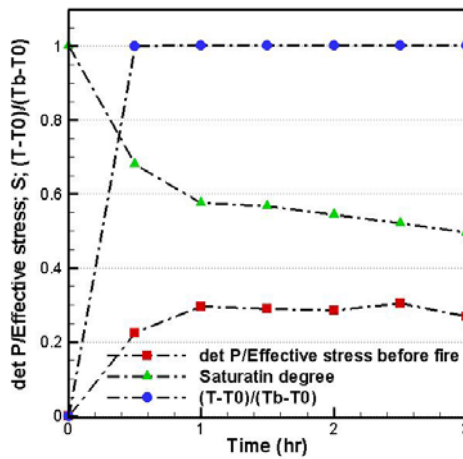


Figure 18 TOUGH2 simulation of fine sand excess pore water pressure change, saturation degree and temperature at the location of 0.01m above the base ($\dot{q}'' = 15 \text{ kW/m}^2$)

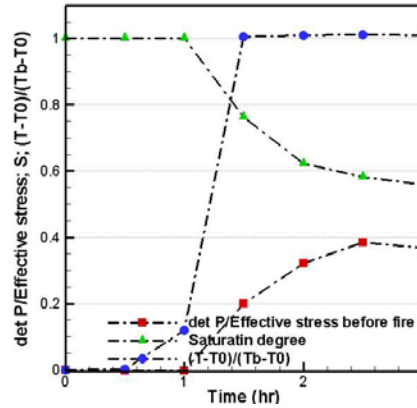


Figure 19 TOUGH2 simulation of fine sand excess pore water pressure change, saturation degree and temperature at the location of 0.2 m above the base ($\dot{q}'' = 15 \text{ kW/m}^2$)

3.2.2 25 kW/m^2 Incident Heat Flux

The same as the analyses before, two sets of experiments are conducted and good repeatability is achieved as shown in Figure 20. A flat temperature distribution is shown at the interface of the two-phase zone and the liquid zone. No convection cell is built up in the liquid zone. In TOUGH2 simulation dry-out occurs at 2.25 hr, and in experiments it occurs at 2.4 hr. The lowest thermocouple (0.05 m) measures temperature of 140°C when $t = 2.5 \text{ hr}$; and 180°C when $t = 3.0 \text{ hr}$. It is also noticed when dry-out occurs in experiments, the vapor front stops propagating and remains at 0.6 m. In Figure 21, the experimental data provides a vapor propagation speed of 0.28 m/hr, the same as TOUGH2 for the first 2.5 hr. Between 2.5 hr and 3.0 hr, a “step” exists in the experiments, while it remains the same vapor propagation speed in TOUGH2. Similar with the 15 kW/m^2 case, the experiments show an intermittently advancing centerline vapor front. The discrepancy between experiments and simulation may be caused by the following reasons.

1) In TOUGH2, the heat flux boundary condition is actually the net basal heat flux. In reality, there exists a thin layer at the base of the soil column (corresponding to the

container thickness), where soil temperature changes from the base temperature (around 400 °C) to boiling temperature or dry-out temperature. When dry-out occurs on the bottom, the soil temperature increases. The base temperature remains nearly the same, resulting in a reduction in the net basal heat flux. However, TOUGH2 is not able to capture this phenomenon, since the heat flux boundary condition is pre-described as an input parameter. So after dry-out occurs, TOUGH2 runs at a larger heat flux than the experiments. This is a possible reason why the vapor front propagation is still seen in TOUGH2 results, while not in experiments.

2) There may be a slight vapor front propagation in experiments. The spacing of thermocouples is 0.1 m, which means if the vapor propagates less than 0.1 m within 0.5 hr, thermocouples there can not capture the movement. It is possible that the vapor front still moves upward in experiments, just within a relatively small range.

3) If it is believed that the occurrence of dry-out stops or slows the vapor front propagation, the 15 kW/m² case seems to be paradoxical, since there is neither dry-out nor a vapor front propagation between 3.5 hr and 4 hr. However, there may be dry-out actually occurring below 0.05 m, but the lowest thermocouple (at 0.05 m) could not capture any change in temperature yet.

Figure 22 and Figure 23 provide TOUGH2 time evolution of the excess pore water pressure, saturation degree and temperature at the location of 0.01 m and 0.2 m above the base. At 0.01 m, dry-out occurs at $t = 2$ hr. Saturation degree decreases to 0.

Before 2 hr, $\frac{\Delta P}{\sigma_{eff_BH}}$ is around 0.35, and decreases to almost 0 after dry-out occurs. At

0.2 m, no dry-out occurs. Vapor front reaches this location at $t = 1$ hr. Saturation degree

changes from 1 to around 0.5. $\frac{\Delta P}{\sigma_{eff_BH}}$ is over 0.4 when boiling occurs at that point, and decreases to 0.2 when dry-out happens at the column bottom.

Based on the discussion before, the vapor front propagation is slowed down after dry-out happens due to a reduced net basal heat flux. The following approach is taken to refine TOUGH2 simulation. The dry-out temperature from TOUGH2 results with the constant boundary condition (as shown in Figure 20) is used to estimate the net basal heat flux. The net basal heat flux is reduced to 10 kW/m² after 2.5 hr. The refined TOUGH2 results are illustrated in Figure 24 and Figure 25, which provide a better agreement with experiments after dry-out occurs. This exercise proves that the discrepancy between the simulated and experimental centerline vapor front propagation speed in Figure 21 results from errors in the specification of the net basal heat flux input in TOUGH2. However, the net basal heat flux and the dry-out temperature on the bottom are coupled variables. Therefore it is difficult to further specify the net basal heat flux without a truly coupled boundary condition also accounting for transient effects.

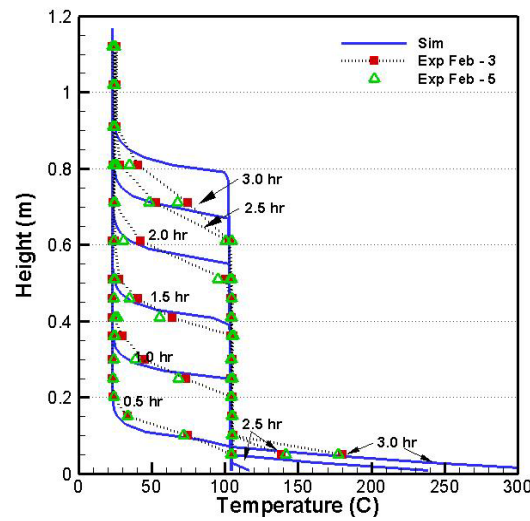


Figure 20 TOUGH2 simulation of centerline temperature for the saturated fine sand soil column compared with experiments ($\dot{q}'' = 25 \text{ kW/m}^2$)

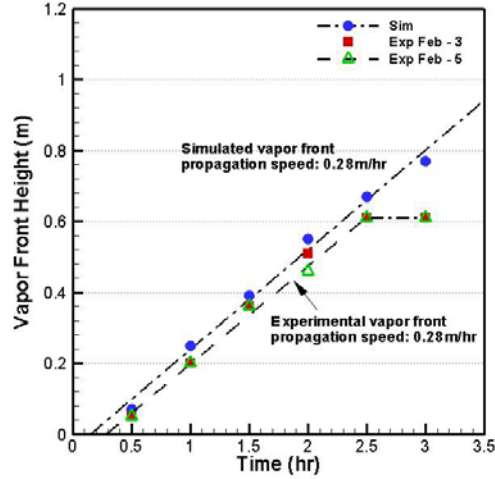


Figure 21 TOUGH2 simulations of the centerline vapor front for the saturated fine sand soil column compared with experiments ($\dot{q}'' = 25 \text{ kW/m}^2$)

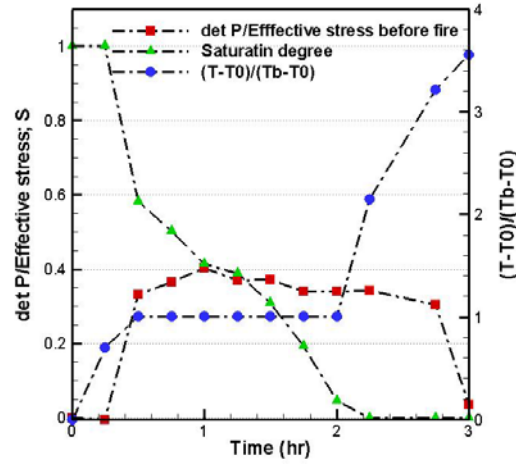


Figure 22 TOUGH2 simulation of fine sand excess pore water pressure change, saturation degree and temperature at the location of 0.01m above the base ($\dot{q}'' = 25 \text{ kW/m}^2$)

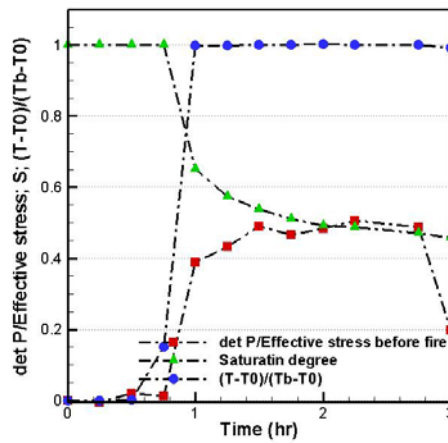


Figure 23 TOUGH2 simulation of fine sand excess pore water pressure change, saturation degree and temperature at the location of 0.2m above the base ($\dot{q}'' = 25 \text{ kW/m}^2$)

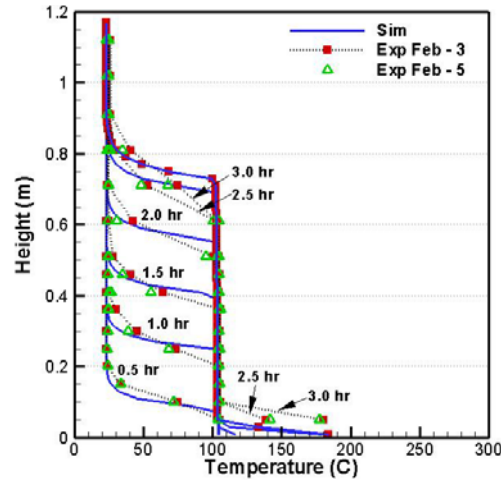


Figure 24 TOUGH2 simulation of centerline temperature for the saturated fine sand soil column compared with experiments ($\dot{q}'' = 10 \text{ kW/m}^2$)

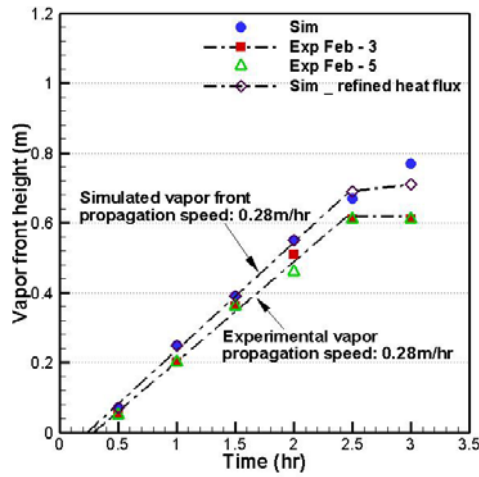


Figure 25 TOUGH2 simulations of the centerline vapor front for the saturated fine sand soil column compared with experiments ($\dot{q}'' = 10 \text{ kW/m}^2$)

3.2.3 35 kW/m² Incident Heat Flux

Figure 26 shows the comparison between the 35 kW/m² incident heat flux experiment and TOUGH2 simulation. In TOUGH2 simulation, dry-out occurs at 1.75 hr, while in experiments it occurs at 1.83 hr. Similar observations are obtained about the intermittence of vapor front propagation when dry-out occurs on the bottom. In this case, the dry-out temperature is 195 °C at $t = 2.0$ hr, and 256 °C at $t = 3.0$ hr. The 35 kW/m² case further proves the discussion in § 3.2.2.

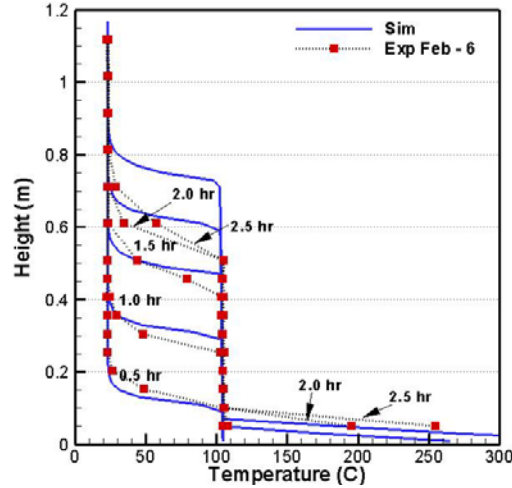


Figure 26 TOUGH2 simulation of centerline temperature for the saturated fine sand soil column compared with experiments ($\dot{q}'' = 35 \text{ kW/m}^2$)

To summarize, no convection cells are developed within the fine sand when it is exposed to intense heat fluxes. The vapor front is built up very fast and dry-out occurs eventually, resulting in much higher temperature in the soil media. Corresponding to that, the excess pore water pressure is larger. As a result, the fine sand structure has a relatively large potential for deformation when tunnel fire occurs.

3.3 Comparison of the Response of Coarse and Fine Sand

The heat and mass transfer pattern is different for the coarse and fine sand media. As expected, the lower permeability of the fine sand suppresses convection. A large convection cell is developed in the coarse sand media, while in the fine sand media there is a steep temperature gradient at the interface of the liquid and two-phase zones and no convection cells. No dry-out region develops in the coarse sand column, while it forms in the fine sand when \dot{q}'' is larger than 25 kW/m^2 . It is also noted that with the same incident heat flux it takes less time for the fine sand to generate the centerline vapor front. For instance, for 15 kW/m^2 incident heat flux, the coarse sand generates the vapor front after 1.5 hr while the fine sand generates the vapor front within the first 0.5 hr.

When exposed to the same incident heat flux, the coarse sand allows a higher vapor front propagation speed, as listed in Table 7. As discussed before, the saturation degree and excess pore water pressure is affected by the heat flux boundary condition; however it is a more strong function of the soil type, or in other words, soil permeability. The fine sand generates higher excess pore water pressure. Detailed comparison is listed in Table 8.

Table 7 Comparison of vapor front propagation speed for coarse/fine sand

	Incident Heat Flux (kW/m ²)	Vapor Front Propagation Speed (m/hr)		Dry-out (Y/N)
		Experiment	TOUGH2	
Coarse Sand	15	0.29	0.25	N
	25	0.42	0.38	N
	35	Porosity/permeability changed. No comparison made.		N
Fine Sand	15	0.18	0.17	N
	25	0.28	0.28	Y (Tough2: t=2.25 hr; Exp.: t=2.4 hr)
	35	0.33	0.29	Y (Tough2: t=1.75 hr; Exp.: t=1.83 hr)

Table 8 Comparison of TOUGH2 excess pore water pressure change, saturation degree of coarse/fine sand

Height: 0.2 m	Saturation degree (after vapor front reaches)	$\frac{\Delta P}{\sigma_{eff-BH}}$	Dry-out region temperature (Experiment)
Coarse 15kW/m ²	0.8	0.17 (1.4 kPa)	---
Coarse 25kW/m ²	0.75	0.19 (1.6 kPa)	---

Fine 15kW/m ²	0.55	0.38 (3.7 kPa)	---
Fine 25kW/m ²	0.45	0.5 (4.9 kPa)	180°C

3.4 Tunnel Fire Simulation

TOUGH2 is validated through detailed comparisons between experiments and simulations in the soil column configuration. To explore soil thermal transient behavior in a realistic geometry, a full scale tunnel model is developed in TOUGH2 as shown in Figure 27. A uniform heat flux of 50 kW/m² is applied to the tunnel lining inner surface. This heat flux is consistent with the large fire size and temperature reported in the literatures in § 1.2.2.

Figure 28 illustrates temperature field development within a coarse sand tunnel. Two convection cells are developed symmetrically above the tunnel. Boiling occurs mainly at the top of the tunnel, with a boiling temperature of 113 °C and pore water pressure before fire of 150 kPa. Comparing with our soil column study, higher boiling temperature is expected due to higher local pressure. At 3 hr, the two-phase zone reaches the tunnel domain boundary. From 1 hr to 3 hr, the vapor front on the top of the tunnel propagates 0.8 m upward. Since the heat flux is larger than the column experiments, higher propagation speed is expected and observed in the tunnel simulation.

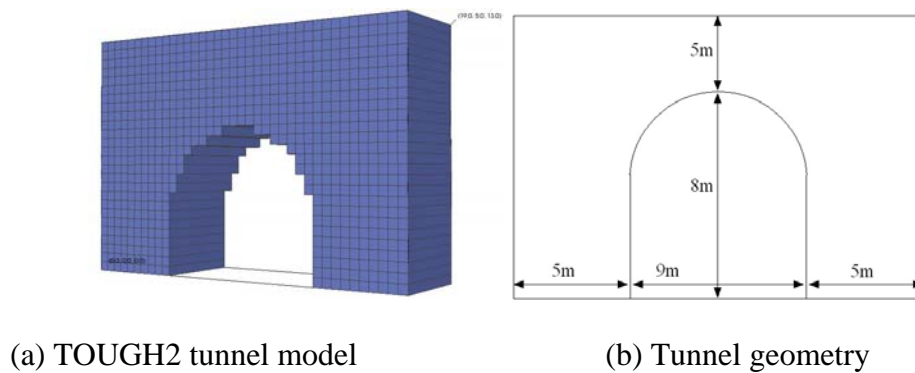


Figure 27 TOUGH2 tunnel model

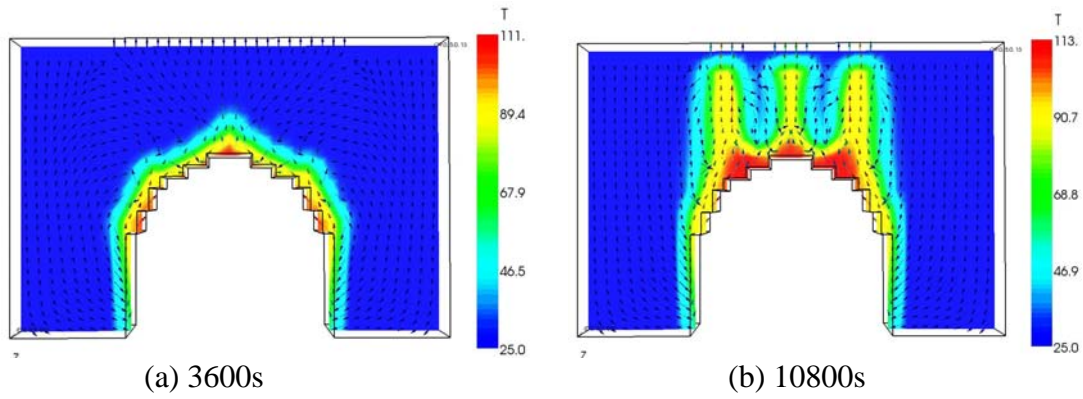


Figure 28 Coarse sand tunnel lining temperature field

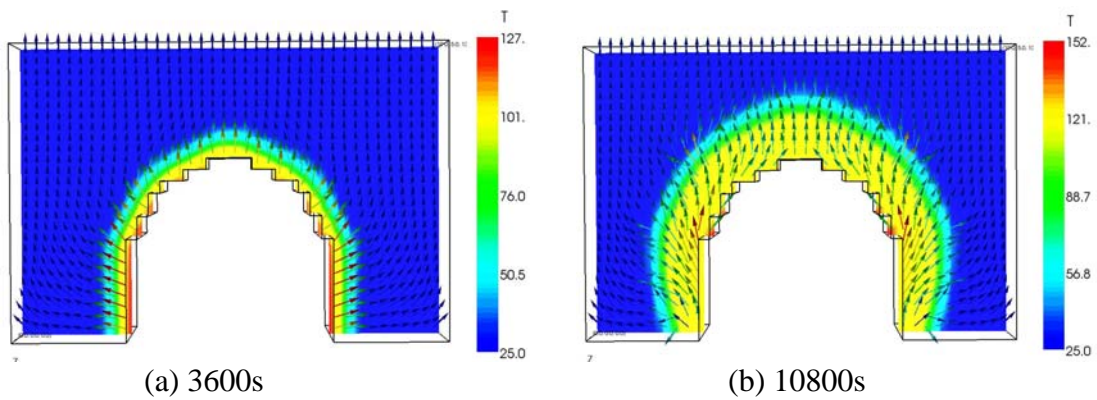


Figure 29 Fine sand tunnel lining temperature field

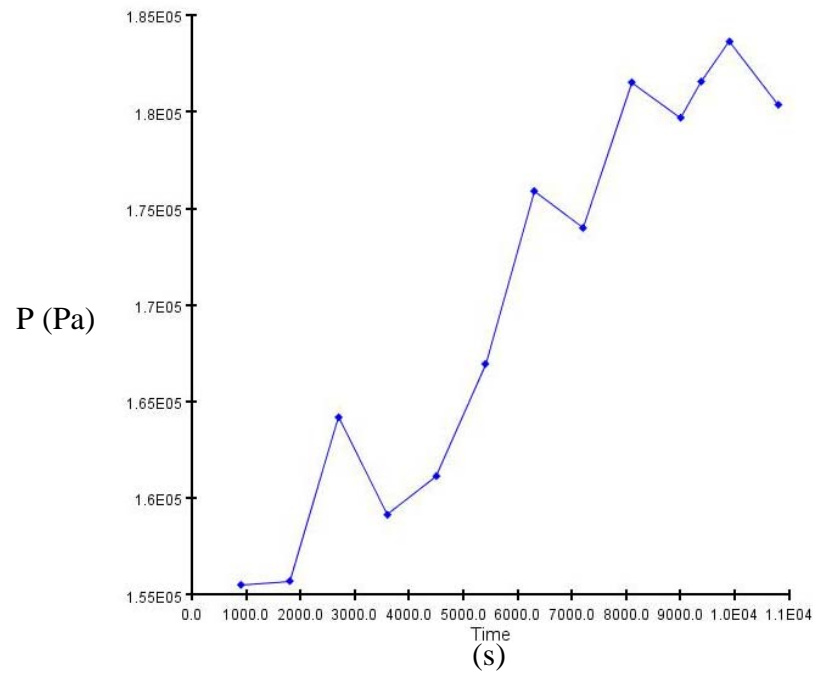


Figure 30 Fine sand pressure history at the tunnel ceiling

For the fine sand tunnel simulation, no convection cells are observed; the two-phase zone expands uniformly surrounding the tunnel geometry. As shown in Figure 29, instead of only on the top, boiling occurs along the whole tunnel lining, even on the bottom of the tunnel. The boiling temperature is 127 °C, with local pressure 220 kPa on the bottom. From 1 hr to 3 hr, the vapor front above the top the tunnel moves up for about 1.5 m. Figure 30 depicts the pressure evolution at the tunnel ceiling. The body of soil at this location is at similar hydro-thermal condition as our column experiments. The excess pore water pressure, ΔP , is 35 kPa; and $\frac{\Delta P}{\sigma_{eff_BH}}$ is around 0.3, comparable with the soil column data.

Chapter 4: Conclusions

This study explores the response of saturated soils (coarse and fine sand) when exposed to intense heat flux from below by both experimental and numerical analyses. For each soil type, three different incident heat flux tests are conducted. A two-dimensional TOUGH2 numerical model is developed to analyze the soil response when exposed to intense heat flux from below. Furthermore, a full scale TOUGH2 model is created to estimate soil behavior in a realistic tunnel fire scenario.

The main results from this study are summarized below:

- 1) The TOUGH2 soil column model has been validated with experimental data based on the temperature profiles and vapor front propagation. Simulation provides insight into the pore water pressure, which is difficult to measure in experiments.
- 2) In coarse sand experiments, a two-zone structure is built up within the soil column, having a liquid zone on the top and a two-phase zone on the bottom. As the vapor front is building up in the two-phase zone, a large convection cell is developed in the liquid zone. The saturation front propagation speed is not a strong function of the incident heat flux. The centerline vapor front propagation speed is 0.29 m/hr when \dot{q}'' equals 15 kW/m², and 0.42 m/hr when \dot{q}'' equals 25 kW/m².
- 3) In fine sand experiments, a three-zone structure is developed when exposed to higher incident heat flux, having a liquid zone on the top, a two-phase zone in the middle, and a vapor zone on the bottom. No convection cells are

developed within the liquid zone. The centerline vapor front propagation speed is 0.18 m/hr when $\dot{q}'' = 15 \text{ kW/m}^2$, 0.28 m/hr when $\dot{q}'' = 25 \text{ kW/m}^2$ and 0.33 m/hr $\dot{q}'' = 35 \text{ kW/m}^2$. Compared to the coarse sand, the vapor front propagation speed of the fine sand is slower, partially due to differences in net heat fluxes to the column. When dry out occurs the centerline vapor front propagation decelerates because of the higher basal temperature and reduced heat flux. The excess pore water pressure, ΔP , is significant in the fine sand and does not significantly change with \dot{q}'' .

- 4) A realistic full scale TOUGH2 model is created to simulate the soil response in a tunnel fire scenario. Boiling temperatures of the soils are higher than the column experiments due to higher local pressure. For the coarse sand, boiling mainly occurs at the top of the tunnel; while for the fine sand boiling occurs uniformly along the tunnel lining. ΔP is observed to be larger than the column experiments with the fine sand, however $\frac{\Delta P}{\sigma_{eff_BH}} = 0.3$ is comparable.

Bibliography

1. Hu, X., *Modeling soil response to intense heating from tunnel fires*, M.S. thesis, University of Maryland at College Park, 2006.
2. Hedefalk, J., Wahlstrom, B. and Rohlen, P., Lessons from the Baku Subway Fire, 3rd Int. Conf. Safety in Road and Rail Tunnels, Nice, France, March 9-11, 1998, pp. 15-28.
3. Lacroix, D., The Mont Blanc tunnel fire: what happened and what has been learned, Proc. 4th Int. Conf. on Safety in Road and Rail Tunnels, Madrid, Spain, April 2-6, 2001, pp. 3-16.
4. http://en.wikipedia.org/wiki/Howard_Street_Tunnel_fire
5. Yong, M. W., *Extreme geotechnical response to high heat from tunnel fires*, M.S. thesis, University of Maryland at College Park, 2004.
6. Campanella, R.G. and Mitchell, J.K., 1968, "Influence of Temperature Variations on Soil Behaviour", Vol. 49, No. SM3, ASCE, pp.709-734.
7. Bau, H.H., Experimental and theoretical studies of natural convection in laboratory-scale models of geothermal systems, Ph.D. thesis, Cornell University, Ithaca, NY, 1980.
8. Bau, H. H. and Torrance, K. E., Low Rayleigh number thermal convection in a vertical cylinder filled with porous materials and heated from below, Transaction of the ASME, Journal of Heat Transfer, Vol. 106, 1982, pp. 166-172.
9. Bau, H.H., Torrance, K.E., Boiling in low-permeability porous materials, International Journal of Heat Mass Transfer, Vol. 25, No. 1, 1982, pp. 45-55.
10. Faust, C.R. and Mercer, J.W., Geothermal reservoir simulation 1. Mathematical

- models for liquid- and vapor- dominated hydrothermal systems, Water resources research, Vol. 15, No.1, 1979, pp.23-30.
11. Roberts, P.J. and Lewis, R.W., An extension of the thermodynamic domain of a geothermal reservoir simulator, Transport in Porous Media, Vol.2, 1987, pp. 397-420.
 12. Ramesh, P.S. and Torrance, K.E., Numerical algorithm for problems involving boiling and natural convection in porous materials, Numerical Heat Transfer, Part B, Vol. 17, 1990, pp.1-24.
 13. Ramesh, P.S. and Torrance, K.E, Stability of boiling in porous media, International Journal of Heat Mass Transfer, Vol. 33, 1990, pp. 1985-1908.
 14. Ramesh, P.S. and Torrance, K.E., Boiling in a porous layer heated from below: effects of natural convection and a moving liquid/two-phase interface, Journal of Fluid Mech., Vol. 257, 1993, pp. 289-309.
 15. Wang, C.Y., Beckermann C. and Fan C., Numerical study of boiling and natural convection in capillary porous media using the two-phase mixture model, Numerical Heat Transfer, Part A, Vol. 26, 1994, pp. 375-398.
 16. Wang, C.Y. and Beckermann C., A two-phase mixture model of liquid-gas flow and heat transfer in capillary porous media - I. Formulation, International Journal of Heat Mass Transfer, Vol, 36, No. 11, 1993, pp. 2747-2758.
 17. Wang, C.Y. and Cheng, P., A multiphase mixture model for multiphase, multicomponent transport in capillary porous media - I. Model development, International Journal of Heat Mass Transfer, Vol, 39, No. 17, 1996, pp. 3607-3618.
 18. Udell, K.S., Heat transfer in porous media heated from above with evaporation, condensation and capillary effects, Journal of Heat and Mass Transfer, Vol. 105,

- 1983, pp. 485-492.
19. Udell, K.S., Heat transfer in porous media considering phase change and capillarity-the heat pipe effect, *Int. J. Heat Mass Transfer*, Vol. 28, No.2, 1985, pp. 485-495.
 20. Shi, B., Boiling heat transfer in porous media with/without chimneys, Ph.D. thesis, University of Illinois at Urbana-Champaign, 1994.
 21. Shi, B., Numerical modeling of boiling heat transfer in porous media, *HTD-Vol. 331, National Heat Transfer Conference*, Vol. 9, ASME 1996, pp. 15-24.
 22. Ulm, F. J., Coussy, O. and Bazant, Z.P., March 1999a, "The Chunnel Fire I – Chemoplastic Softening in Rapidly Heated Concrete", *Journal of Engineering Mechanics*, ASCE, 125(3), pp 272-282.
 23. Ulm, F. J., Acker, P. and Levy, M., March 1999b, "The Chunnel Fire II – Analysis of Concrete Damage", *Journal of Engineering Mechanics*, ASCE, 125(3), pp 283-289.
 24. Carvel, R.O., Drysdale, D.D., The influence of tunnel geometry and ventilation on the heat release rate of a fire, *Fire Technology*, Vol. 40, 2004, pp.5-26.
 25. Ingason, H., Model scale railcar fire tests, *Fire Safety Journal*, Vol.42, 2007, pp. 271-282.
 26. Megret, O., Vauquelin, O, A model to evaluate tunnel fire characteristics, *Fire Safety Journal*, Vol. 34, 2000, pp.393-401.
 27. McGrattan, K.B., Hamins, A., Numerical simulation of the Howard street tunnel fire, Baltimore, Maryland, July 2001, NIST technical report.
 28. Carrier, W.D., 2003, "Goodbye, Hazen; Hello, Kozeny-Carman", *ASCE, Journal of Geotechnical and Geoenvironmental Engineering*, November 2003, pp 1054-1056.
 29. William Lambe, T., Whitman, R.V., *Soil Mechanics*, John Wiley & Sons, Inc., 1969.

30. TOUGH2 Userguide.
31. Fredlund, D. G. and Rahardjo, H., Soil mechanics for unsaturated soils, John Wiley & Sons, Inc., 1993.